


## RESEARCH ARTICLE

# Visualizing the deep cerebellar nuclei using quantitative susceptibility mapping: An application in healthy controls, Parkinson's disease patients and essential tremor patients

Youmin Zhang<sup>1</sup> | Pei Huang<sup>2</sup> | Xinhui Wang<sup>1</sup> | Qiuyun Xu<sup>3</sup> | Yu Liu<sup>1</sup> |  
 Zhijia Jin<sup>1</sup> | Yan Li<sup>1</sup> | Zenghui Cheng<sup>1</sup> | Rongbiao Tang<sup>1</sup> | Shengdi Chen<sup>2</sup> |  
 Naying He<sup>1</sup> | Fuhua Yan<sup>1</sup>  | E. Mark Haacke<sup>1,3,4</sup>

<sup>1</sup>Department of Radiology, Ruijin Hospital, Shanghai Jiao Tong University School of Medicine, Shanghai, China

<sup>2</sup>Department of Neurology, Ruijin Hospital, Shanghai Jiao Tong University School of Medicine, Shanghai, China

<sup>3</sup>Department of Biomedical Engineering, Wayne State University, Detroit, Michigan, USA

<sup>4</sup>Department of Radiology, Wayne State University, Detroit, Michigan, USA

## Correspondence

Fuhua Yan and Naying He, Department of Radiology, Ruijin Hospital, Shanghai Jiao Tong University School of Medicine, No.197 Ruijin Er Road, Shanghai, 200025, China.  
 Email: [yfh11655@rjh.com.cn](mailto:yfh11655@rjh.com.cn), [inayinghe.com](mailto:inayinghe.com)

Shengdi Chen, Department of Neurology, Ruijin Hospital, Shanghai Jiao Tong University School of Medicine, No.197 Ruijin Er Road, Shanghai, 200025, China.  
 Email: [ruijincsd@126.com](mailto:ruijincsd@126.com)

## Funding information

National Natural Science Foundation of China, Grant/Award Number: 81971576; National Key R&D Program of China, Grant/Award Numbers: 2022YFC2009905, 2022YFC2009900

## Abstract

The visualization and identification of the deep cerebellar nuclei (DCN) (dentate [DN], interposed [IN] and fastigial nuclei [FN]) are particularly challenging. We aimed to visualize the DCN using quantitative susceptibility mapping (QSM), predict the contrast differences between QSM and T2\* weighted imaging, and compare the DCN volume and susceptibility in movement disorder populations and healthy controls (HCs). Seventy-one Parkinson's disease (PD) patients, 39 essential tremor patients, and 80 HCs were enrolled. The PD patients were subdivided into tremor dominant (TD) and postural instability/gait difficulty (PIGD) groups. A 3D strategically acquired gradient echo MR imaging protocol was used for each subject to obtain the QSM data. Regions of interest were drawn manually on the QSM data to calculate the volume and susceptibility. Correlation analysis between the susceptibility and either age or volume was performed and the intergroup differences of the volume and magnetic susceptibility in all the DCN structures were evaluated. For the most part, all the DCN structures were clearly visualized on the QSM data. The susceptibility increased as a function of volume for both the HC group and disease groups in the DN and IN ( $p < .001$ ) but not the FN ( $p = .74$ ). Only the volume of the FN in the TD-PD group was higher than that in the HCs ( $p = .012$ ), otherwise, the volume and susceptibility among these four groups did not differ significantly. In conclusion, QSM provides clear visualization of the DCN structures. The results for the volume and susceptibility of the DCN can be used as baseline references in future studies of movement disorders.

**Abbreviations:** ANOVA, one-way analysis of variance; CNR, contrast-to-noise ratio; DCN, deep cerebellar nuclei; DGM, deep gray matter; DN, dentate nucleus; EN, emboliform nucleus; ET, essential tremor; FA, flip angle; FN, fastigial nucleus; GN, globose nucleus; HC, healthy control; ICC, intraclass correlation coefficient; IN, interposed nucleus; MDS-UPDRS, Movement Disorder Society Unified Parkinson's Disease Rating Scale; MMSE, Mini-Mental State Examination; MRI, magnetic resonance imaging; PD, Parkinson's disease; PDW, proton density weighted; PIGD, postural instability/gait difficulty; PSD, proton spin density; QSM, quantitative susceptibility mapping; ROI, region-of-interest; SNR, signal-to-noise ratio; STAGE, strategically acquired gradient echo; SWI, susceptibility weighted imaging; T1W, T1 weighted; T2\*W, T2 star weighted; TD, tremor dominant; TE, echo time; TR, repetition time; WM, white matter.

Youmin Zhang and Pei Huang made equal contributions.

This is an open access article under the terms of the [Creative Commons Attribution-NonCommercial-NoDerivs](https://creativecommons.org/licenses/by-nc-nd/4.0/) License, which permits use and distribution in any medium, provided the original work is properly cited, the use is non-commercial and no modifications or adaptations are made.

© 2022 The Authors. *Human Brain Mapping* published by Wiley Periodicals LLC.

## KEYWORDS

deep cerebellar nuclei, essential tremor, Parkinson's disease, quantitative susceptibility mapping

## 1 | INTRODUCTION

There are four pairs of nuclei embedded in the cerebellum. They are the fastigial nuclei (FN), the globose/emboliform nuclei (or interposed nuclei, IN), and the dentate nuclei (DN; Pruthi et al., 2021; Slaughter & Nashold Jr., 1968). The deep cerebellar nuclei (DCN) play a strategic role in cerebellar function as they integrate the excitatory and inhibitory signals to provide the final output of the cerebellar circuits. Except for vestibular information, the DCN are the predominant source of output from the cerebellar circuitry (Manto & Oulad Ben Taib, 2010).

The DCN are involved in the pathophysiology underlying many movement disorders (Deistung et al., 2016; Ibrahim et al., 2021; Kakita et al., 1994; Koeppen et al., 2007). Specifically, the DCN hold a crucial position in the cerebello-thalamo-cortical circuit which is closely associated with the occurrence of motor symptoms in Parkinson's disease (PD) and essential tremor (ET) (Helmich et al., 2012; Nicoletti et al., 2020). As the two most common neurological movement disorders (Lim et al., 2019; Louis & Ferreira, 2010), PD and ET present with similar clinical features whose differential diagnosis could be challenging for neurologists in the early stage, especially between the PD motor phenotypes and ET. Despite the availability of other imaging techniques to distinguish patients with PD and ET, such as positron emission tomography (PET) and single photon emission computed tomography (SPECT), the high cost of PET/SPECT limits their widespread application in clinical practice.

The DN is one of the deep gray matter (DGM) structures with high iron content (Acosta-Cabronero et al., 2016; Aoki et al., 1989; Burgetova et al., 2021; Hallgren & Sourander, 1958; Li et al., 2014). According to previous studies, other DCN also appear to have high levels of iron since they show a signal loss on T2\* weighted (T2\*W) imaging similar to the DN (Dimitrova et al., 2006) or susceptibility weighted imaging (SWI) (Diedrichsen et al., 2011). It has been confirmed that iron is the dominant contributor to magnetic susceptibility in gray matter and can be assessed with Quantitative Susceptibility Mapping (QSM) (Deistung et al., 2017; Langkammer et al., 2012; Zheng et al., 2013). Moreover, QSM measures correlate well with postmortem measures of iron content (Bilgic et al., 2012; Chai et al., 2015; Hallgren & Sourander, 1958; Persson et al., 2015). Compared with magnitude images or R2/R2\* maps, QSM is not only a promising approach with superior sensitivity and specificity to measure iron content in vivo, but also has excellent contrast and reflects the anatomy of those DGM structures with high iron content (Barbosa et al., 2015; Deistung et al., 2013; Du et al., 2016; Haacke et al., 2015).

A growing body of literature has attempted to characterize the iron deposition patterns of the DN in PD and ET, but the conclusions are varied across studies. Numerous studies have shown increased

iron content in the DN putatively correlating with the presence of tremor, thereby offering the potential to distinguish PD motor subtypes (Chen et al., 2020; Guan, Xuan, Gu, Xu, et al., 2017; He, Huang, et al., 2017). However, a recent study evaluated the iron deposition in HCs, PD, and ET and found no evidence of iron deposition differences among these three groups (Pietracupa et al., 2021).

In the past few decades, many groups have explored the properties of the DN (see Table S1). These studies rarely involved the other DCN due to their contrast on conventional imaging being low making them difficult to find. In this study, we hypothesized that all the DCN could be visualized on the QSM data at 3T with a high contrast-to-noise ratio (CNR) and that the DCN volume and susceptibility could be used to differentiate PD subtypes, specifically TD-PD and PIGD-PD patients from ET patients. Therefore, our goal was to visualize the DCN using QSM; predict the contrast differences between QSM and T2\*W imaging, quantify the DCN volume and susceptibility as a function of age and compare the results between different movement disorder populations and HCs.

## 2 | MATERIALS AND METHODS

### 2.1 | Participants

This study was approved by the local ethics committee at Ruijin Hospital, Shanghai Jiao Tong University School of Medicine and written informed consent was obtained from all participants. A total of 217 subjects (85HCs, 132 patients) (Figure 1) were enrolled. All HCs were recruited from the health examination center from April 2020 to December 2021 according to the following inclusion criteria: (1) no personal or family history of neurological or psychiatric diseases, (2) no neurological and/or mental disease, no history of taking psychotropic drugs; (3) no cardiovascular or cerebrovascular disease; and (4) no MRI contraindications such as a cardiac pacemaker, insulin pump, artificial heart valve, coronary stent, steel nail plate or contraceptive ring implantation history. All patients were consecutively recruited from the Movement Disorders Clinic of Ruijin Hospital, Shanghai Jiao Tong University School of Medicine from April 2020 to February 2021 with the exclusion criteria: (1) Mini-Mental State Examination (MMSE) score < 24; (2) a history of cerebrovascular disease (e.g., infarction, hemorrhage), brain tumor, head trauma or any other type of psychiatric disorders; (3) a history of medication known to cause parkinsonism or affect clinical assessment; or (4) any contraindications to having an MRI examination.

PD patients were diagnosed based on the Movement Disorder Society (MDS) Clinical Diagnostic Criteria (Postuma et al., 2015) and the diagnosis of ET was made according to the consensus statement of the MDS on tremors (Bhatia et al., 2018). Disease duration was

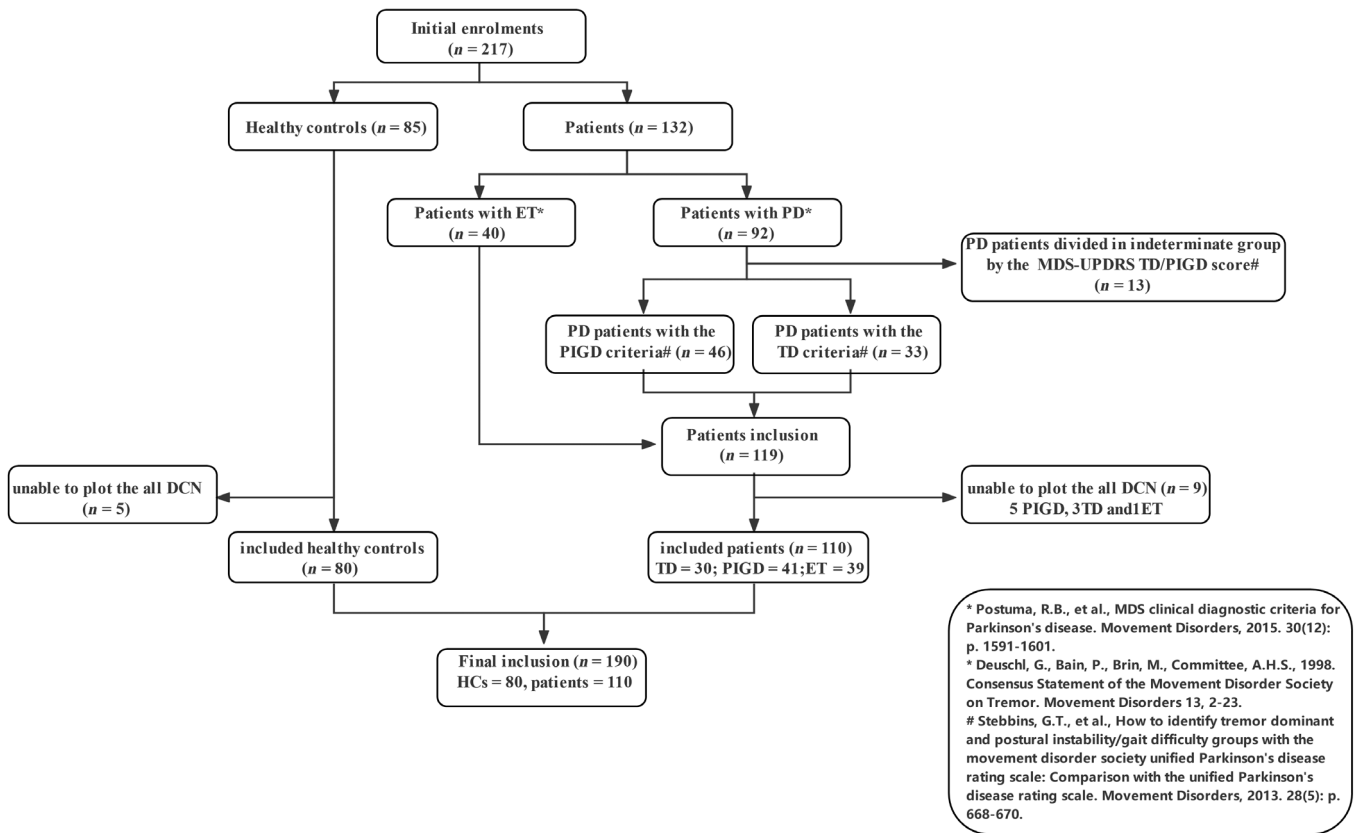


**FIGURE 1** Summary of participants' recruitment and exclusions

collected for all patients, and the Hoehn & Yahr stage and the MDS Unified Parkinson's Disease Rating Scale Part-III (UPDRS-III) were obtained for all PD patients. In the present study, we divided PD patients into three subgroups: TD-PD ( $n = 33$ ), PIGD-PD ( $n = 46$ ), and indeterminate ( $n = 13$ ) by calculating the MDS-UPDRS mean-TD/mean-PIGD score (Stebbins et al., 2013). If the resultant ratio was  $>1.15$  then the patient was classified as TD-PD. If the ratio was  $<0.90$ , then the patient was classified as PIGD-PD. If the ratio was between 0.90 and 1.15, then the patient was classified as indeterminate. Given that the sample size of the indeterminate group was small, we excluded this group when performing the intergroup analyses.

## 2.2 | MRI data acquisition

All scans were performed on a 3T MR scanner (Ingenia, Philips Healthcare, Netherlands) equipped with a 15-channel head coil. Ear-plugs and foam cushions were provided for all participants to remain comfortable and reduce motion artifacts during scanning. The three-dimensional multi-echo strategically acquired gradient echo (STAGE) imaging protocol was used to acquire the data. STAGE is a multi-echo, multi-flip angle method designed to generate a variety of qualitative and quantitative images such as T1,  $T_2^*$ ,  $R_2^*$ , proton density, and susceptibility maps (Chen et al., 2018; Haacke et al., 2020; Wang et al., 2018). The imaging parameters were: echo times

(TE) = 7.5 ms, 15 ms, and 22.5 ms, repetition time (TR) = 27 ms, flip angles (FA) =  $6^\circ$  and  $27^\circ$ , an in-plane resolution =  $0.67 \text{ mm} \times 1 \text{ mm}$  (interpolated to  $0.67 \text{ mm} \times 0.67 \text{ mm}$ ), FOV =  $256 \text{ mm} \times 192 \text{ mm}$ , pixel bandwidth = 189 Hz/pixel, matrix =  $348 \times 192$ , slice thickness = 1.34 mm, partial Fourier factor = 87.5%, elliptical sampling = on, and total scan time = 9 min (including both FA scans). Additionally, diffusion weighted imaging and T2-weighted fluid-attenuated inversion recovery images were acquired to screen for cerebrovascular disease. All scans were acquired parallel to the anterior commissure-posterior commissure line.

## 2.3 | Data processing

### 2.3.1 | Reconstruction of QSM, T1, PSD, and $T_2^*/R_2^*$ maps

The QSM, T1 maps, proton spin density (PSD) maps, and  $T_2^*/R_2^*$  maps were obtained using STAGE 2.7 software (SpinTech MRI, Birmingham Farms, MI, USA) based on the methods introduced by Chen et al. (2018) and Wang et al. (2018). The use of both the proton density weighted (PDW,  $6^\circ$ ) and T1 weighted (T1W) ( $27^\circ$ ) images makes it possible to correct for the radiofrequency transmit field and receive coil variations and create the QSM, T1, PSD, and  $T_2^*/R_2^*$  maps.

### 2.3.2 | Determination and delineation of the regions of interest

We determined the presence of the DCN on QSM data based on their known anatomical locations and several well-established MRI atlases of the DCN (Dimitrova et al., 2002; Dimitrova et al., 2006; Naidich et al., 2009; Pruthi et al., 2021). The DN is located in the bilateral cerebellar hemispheres; the FN is present most medially at the roof of the fourth ventricle and the IN (including the emboliform nucleus [EN] and the globose nucleus [GN]) lies between the DN and the FN; the GN is closer to the FN, while the EN is more lateral/ventral/cranial and adjacent to the DN. Given that the EN and GN are adjacent to each other and appear to fuse, we considered them as one single structure in this work (although the EN and GN are visible in 3 to 4 slices, usually, they are connected in 1 to 2 of these slices). Similarly, the bilateral FN often appear connected; therefore, we also considered them as one single structure. All the DCN structures were manually evaluated on the axial images based on the QSM data using Signal Processing in NMR (SPIN) software (SpinTech, Inc, Bingham Farms, MI, USA).

The criteria for drawing the ROI of each structure were as follows: (1) boundaries were drawn on QSM data axial slices and saved as ROIs; (2) QSM data were displayed in three orientations (axial, coronal, and sagittal planes) simultaneously when drawing the ROIs to ensure the correct boundaries were obtained (Figure 2); (3) EN and GN were plotted as a single ROI, the ROIs only drawn where the QSM data showed a high signal; (4) all images (QSM, T1maps, PSD maps) were zoomed by a factor of four at the same center point to ensure a clear and identical overlap of each structure on each image type; (5) T1W (27°) structural images were used as an anatomical

reference to avoid the fourth ventricle; and, lastly, (6) vessels were avoided when drawing the boundaries. The mean magnetic susceptibility of each DCN was calculated from the QSM data and the DCN volume was calculated as the number of voxels within the ROIs multiplied by the volume of a single voxel. DCN ROIs were manually delineated by a single rater who was blinded to all clinical information. To assess the reliability of drawing the ROIs, the second rater (who was blinded to any identifiers) also drew the ROIs for 80 subjects that were randomly selected from the four groups (20 cases in each group) to assess inter-rater reliability. The final boundaries were reviewed by the same two raters; if there were disagreements, the two raters reviewed the data and came to a consensus regarding the boundaries.

### 2.4 | Simulating DCN contrast with surrounding white matter

Simulations were performed using tissue parameters for 3 T imaging. To understand the contrast in the DCN, we performed a theoretical simulation of the signal from white matter (WM) and the DN using Equation (1). This lack of contrast between the DN and WM can be predicted by incorporating the spin density, T1, and T2\* values into the usual signal intensity formula

$$S(\theta, TE) = \rho_0 \sin \theta \frac{(1 - E_1)}{(1 - E_1 \cos \theta)} E_2 \quad (1)$$

where,  $E_1 = e^{-TR/T1}$  and  $E_2 = e^{-TE/T2^*}$  and  $\theta_E$  is the Ernst angle, the angle at which the signal is a maximum. The high iron deposition of the DN causes it to have a reduced T2\* relative to the surrounding

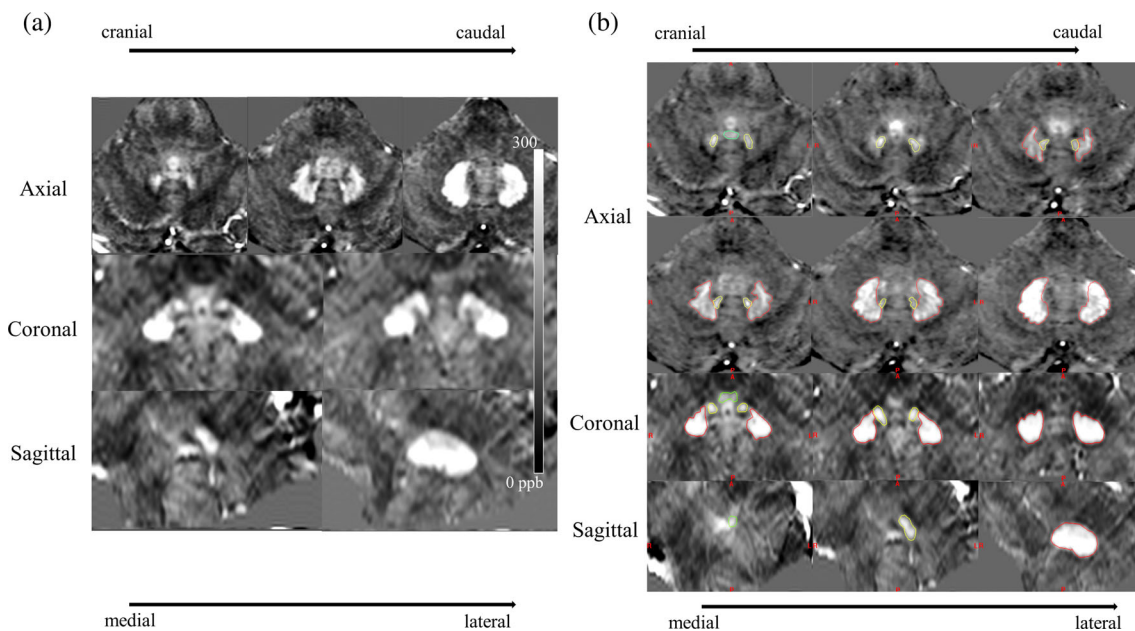


**FIGURE 2** Identification of the deep cerebellar nuclei (DCN) on QSM data. The DCN are visible as hyper-intensities on QSM. Dentate nuclei (DN), interposed nuclei (IN) and fastigial nuclei (FN) are displayed without (a) and with (b) boundaries from the axial, coronal and sagittal plane. Red boundaries: DN; yellow boundaries: IN; and green boundaries: FN

WM. Given that the water content of the DN is higher than that of the WM, the effective spin density is thereby reduced making the DN appear more like WM at short TE. That is, eventually, there will be a TE value where

$$\rho_{WM}e^{(-TE/T2_{WM}^*)} = \rho_{DN}e^{(-TE/T2_{DN}^*)} \quad (2)$$

There is no single gold standard for spin density, but reported values are reasonably close to each other. For example, Mezer et al. (2016) reported a proton spin density (PSD) of  $0.74 \pm 0.07$  for WM and  $0.83 \pm 0.06$  for GM. Abbas et al. (2015) reported a PSD of  $0.7 \pm 0.01$  for WM, and PSD values of various DGM to be:  $0.83 \pm 1.3$  for caudate (head),  $0.77 \pm 1.9$  for globus pallidus,  $0.82 \pm 1.3$  for putamen,  $0.82 \pm 1.9$  for the hippocampus and  $0.82 \pm 1.7$  for the thalamus. Also, based on our measurements, we noticed that the PSD of WM ranges from 0.68 to 0.74 depending on the location. For example, the WM in the corona radiata has a higher PSD value (about 9%) than the frontal WM or the WM near the peripheral cortex. After evaluating the WM throughout the brain, we found that on average  $PSD_{WM} = 0.84$   $PSD_{GM}$  and  $PSD_{GM} = 0.84$   $PSD_{CSF}$ . Given that there is little to no contrast in the TE = 7.5 ms images, the PSD for the DN can be found in the expression  $PSD_{DN} = PSD_{WM} \exp(TE * \Delta R_2^*)$ . With  $\Delta R_2^* = 11/s$  and  $PSD_{WM} = 0.74$ , this yields a  $PSD_{DN} = 0.80$ . Therefore, for simulation purposes, we chose to use the two limits of (0.74, 0.80) and (0.68, 0.84) for the PSD of (WM, DN) to cover all possible ranges.

For the choice of T1 values at 3T, Dieringer et al. (2014) reported a T1 of  $911 \pm 15$  ms for WM, and Wright et al. (2008) reported a T1 of  $840 \pm 50$  ms for WM. Despite these variations, we used a T1 of 900 ms for WM, which has been used recently in the work of Wang et al. (2018). Based on our measurements, the DN has about 0.2 ppm susceptibility which causes a major decrease in T1 and, practically, it appears to equal WM. Therefore, we also used a T1 of 900 ms for DN in this simulation. Multiple researchers (Weiskopf et al., 2013; Zhou et al., 2020) have reported a T2\* of 50 ms for WM. In our measurements, we found the range of T2\* for DN was between 25 ms and 50 ms. However, sometimes the capsule (the cauliflower-like edges) of the DN have slightly higher iron content and lower T2\*, therefore, we chose to use the range of 20 ms to 40 ms (using increments of 5 ms) for T2\* to simulate the signal decay for a given TE. We took these as reasonably representative of the IN as well since it is much easier to measure contrast in the DN with the surrounding WM.

## 2.5 | Statistical analysis

The clinical characteristics of the HC, ET, PIGD-PD and TD-PD groups were compared using one-way analysis of variance (ANOVA) with post hoc Bonferroni correction for multiple comparisons. Differences in sex ratio between groups were tested with chi-squared tests. Inter-group comparisons of the mean volume and susceptibility of all the DCN were performed using ANOVA with Bonferroni correction for four groups. Linear regression models were applied to evaluate the correlation between the mean volume and susceptibility of the right

and left DCN and the mean volume and susceptibility of the bilateral DCN and age in these four groups, as well as the correlation between the volume and susceptibility. An intraclass correlation coefficient (ICC) was calculated to assess the interrater reliability of the delineation of the ROIs. An ICC of 0.81 to 1.00 was considered excellent agreement, 0.61 to 0.80 good agreement, 0.41 to 0.60 moderate agreement, 0.21 to 0.40 fair agreement, and 0.20 or less poor agreement. All tests were 2-tailed, and *p* values <.05 were considered to indicate statistical significance. All statistical analyses were performed using IBM SPSS Statistics (version 24; IBM Corp., Armonk, NY).

## 3 | RESULTS

### 3.1 | Demographic and clinical characteristics of participants

Fourteen subjects (5 HCs, 5 PIGD-PD, 3 TD-PD, and 1 ET) were excluded given that the IN and FN could not be clearly defined. Also, the indeterminate group of PD patients (*n* = 13) was excluded. A total of 190 subjects were finally included in this study: 80 HCs, 39 ET, 41 PIGD-PD and 30 TD-PD. Demographic and clinical characteristics are given in Table 1. There were no statistically significant differences between groups regarding age and sex; however, ET patients had a longer disease duration (*p* < .001) compared to PIGD-PD and TD-PD patients. The PIGD-PD group had a significantly higher Hoehn & Yahr stage (*p* < .025) compared to TD-PD patients.

### 3.2 | Imaging of the DCN

To display the DCN clearly, we reformatted the images into a plane that revealed all the DCN simultaneously using SPIN software (Figure 3). The DCN were visible on the QSM data for all the final recruited subjects (Figure 4). Except for the susceptibility of the FN in the PIGD-PD group (ICC, 0.684), in the four groups, the ICCs for agreement in volume and susceptibility measurements between raters were more than 0.7; all results showed good agreement between raters. For some structures, there was a significant bias which caused the absolute confidence intervals to become quite large. However, the confidence intervals of the consistency between raters remained small similar to those seen when there was little bias between the raters (see Table S2).

### 3.3 | Contrast between the DCN and WM

One of the key findings in this work was that the visibility of the DCN was highest with QSM compared to T1W or T2\*W images or R2\* (1/T2\*) maps (Figure 5). Visualizing the DCN on the T1W images was generally not possible for the TE = 7.5 ms images. Once a longer TE was used, the DN/IN revealed themselves as having a lower signal as expected because of their lower T2\* values. The T1 map itself showed

**TABLE 1** Demographic and clinical information of four groups

	HC (n = 80)	ET (n = 39)	PIGD- PD (n = 41)	TD- PD (n = 30)	p-value	Bonferroni correction					
						HC versus ET	HC versus PIGD- PD	HC versus TD-PD	ET versus PIGD- PD	ET versus TD-PD	PIGD- PD versus TD-PD
Age (mean ± SD)	60.5 ± 6.6	61.3 ± 8.2	64.0 ± 9.7	63.6 ± 7.4	.066	-	.119	.375	.730	-	-
Sex (male/female)	40/40	19/20	27/14	18/12	.299	-	-	-	-	-	-
MDS-UPDR-III score <sup>a</sup>	NA	NA	24.4 ± 13.9	24.4 ± 14.7	.995	-	-	-	-	-	-
Mean-TD/mean- PIGD score	NA	NA	0.3 ± 0.2	2.3 ± 0.7	.000*	-	-	-	-	-	-
Hoehn & Yahr stage	NA	NA	2.0 ± 0.08	1.6 ± 0.5	.025*	-	-	-	-	-	-
Disease duration, years	NA	8.3 ± 6.8	3.6 ± 2.4	4.0 ± 2.9	.000*	-	-	-	.000*	.001*	-

Abbreviations: ET, essential tremor; HCs, health controls; TD-PD, tremor dominant PD; PIGD, postural instability/gait difficulty PD; MDS-UPDRS III, third part of the MDS-UPDRS; NA, not available.

<sup>a</sup>Calculated from the MDS-UPDRS III.

\*p values <.05 were considered significant.

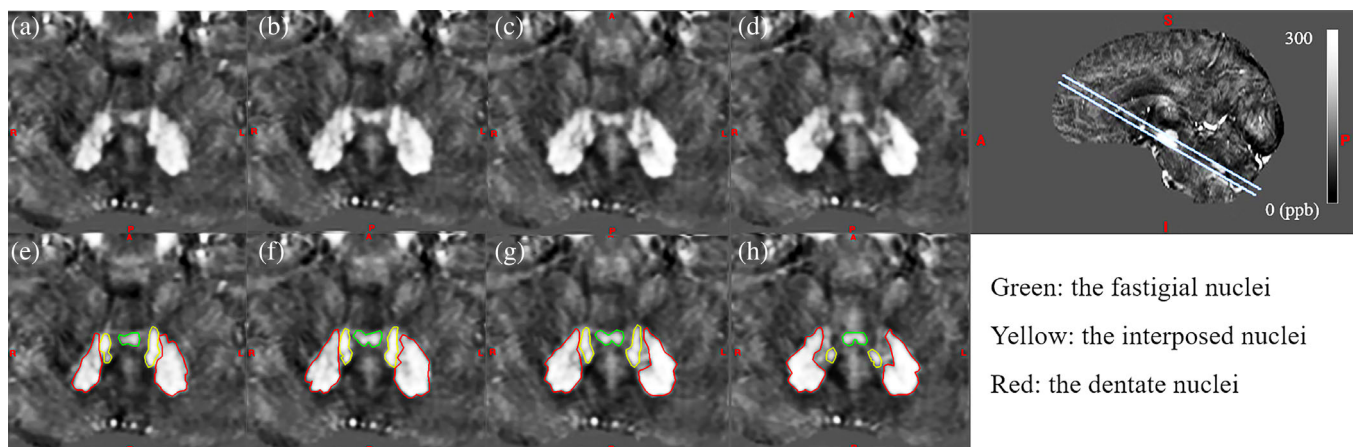


**FIGURE 3** Showing the deep cerebellar nuclei (DCN) with reformatted QSM images. These images were created from the original data by connecting the substantia nigra and dentate nucleus along a line in the sagittal images (rightmost), this pseudo-axial plane is able to show the all DCN simultaneously. (a–d) Show the DCN without boundaries and (e–h) show the DCN with boundaries. Red boundaries: Dentate nuclei; yellow boundaries: Interposed nuclei; and green boundaries: Fastigial nuclei

that the DCN had the same effective T1 as the surrounding WM. The measured value of the T2\* for the DCN as a whole was found to range from 20 ms to 40 ms.

Using a TR of 27 ms, we found that the crossover varied from TE = 2.6 ms to 42.3 ms as T2\* varied from 20 to 40 ms (Figure 6). At longer TE, the DCN can be seen with reduced signal intensity, and the negative contrast relative to WM increases accordingly in agreement with our simulations of the signal as a function of TE and FA (Figure S1). Overall, the DN and IN tend to have higher iron content than the FN; however, when the FN has high iron content it behaves similarly to the DN and IN in terms of its contrast behavior.

Measuring the noise in the QSM data in a variety of uniform regions revealed a maximum noise of  $\sigma_{\text{QSM}} = 8$  ppb while that in the R2\* maps was found to be  $\sigma_{\text{R2}^*} = 1.5/s$ . Therefore, CNR in the QSM

data is the susceptibility value in ppb divided by 8 ppb and the CNR for the R2\* maps for gray matter relative to white matter is  $(\text{R2}^* - 20/s) = \Delta\text{R2}^*$  divided by  $1.5/s$  where  $20/s$  is the R2\* value of WM. For the DN/IN with susceptibility of say 80 ppb, this gives a CNR of 10:1 while for  $\text{R2}^* = 30/s$  then,  $\Delta\text{R2}^* = 10/s$ , and the CNR is only 6.5:1. The FN has an R2\* of about 15/s and a  $\Delta\text{R2}^*$  of only 5/s making it more difficult to see.

### 3.4 | Intergroup differences in the DCN volumes and susceptibility values

The volume and susceptibility of the DCN in all four groups (HCs, ET, PIGD-PD, and TD-PD) are summarized in Table 2. The volume of the

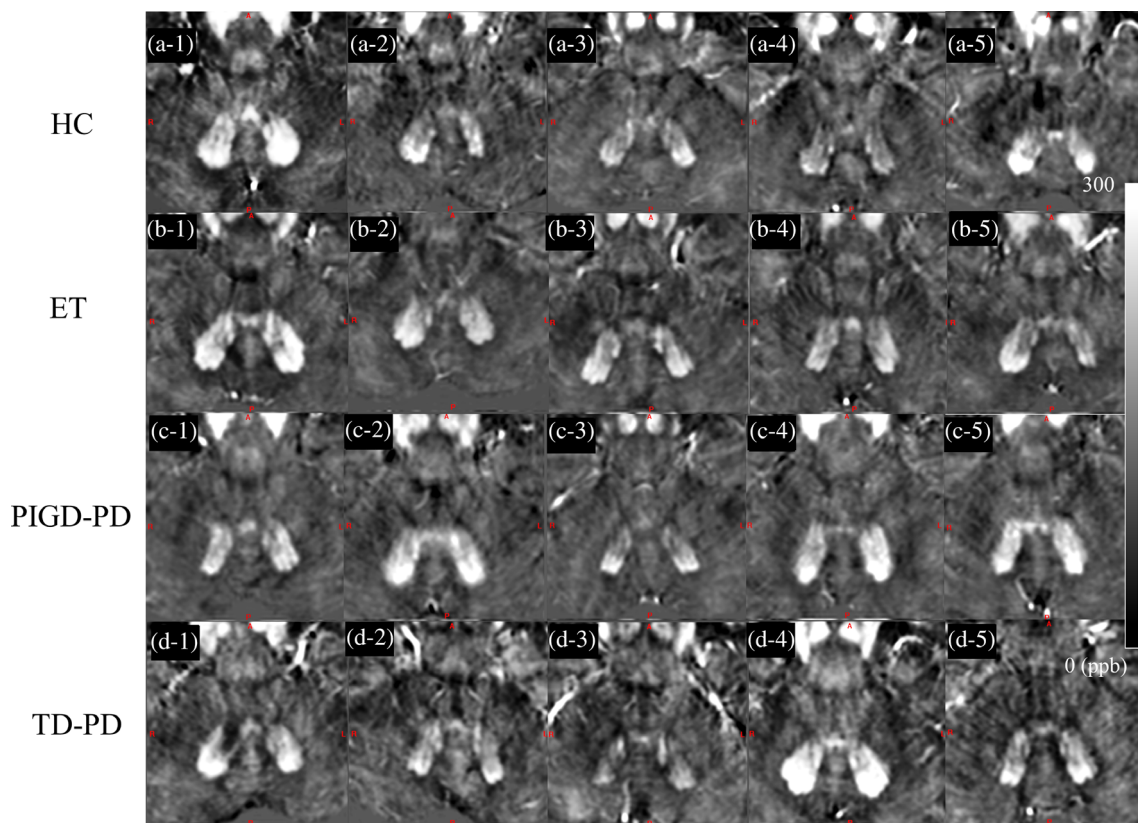


**FIGURE 4** Deep cerebellar nuclei (DCN) of the HC, ET and PD subtypes on reformatted QSM images. (a1–a5) five subjects of HC, (b1–b5) five subjects of ET, (c1–c5) five subjects of PIGD-PD, (d1–d5) five subjects of PIGD-PD. HC, healthy controls; ET, essential tremor; PIGD-PD, PD patients with postural instability/gait difficulty; TD-PD, PD patients with tremor dominance

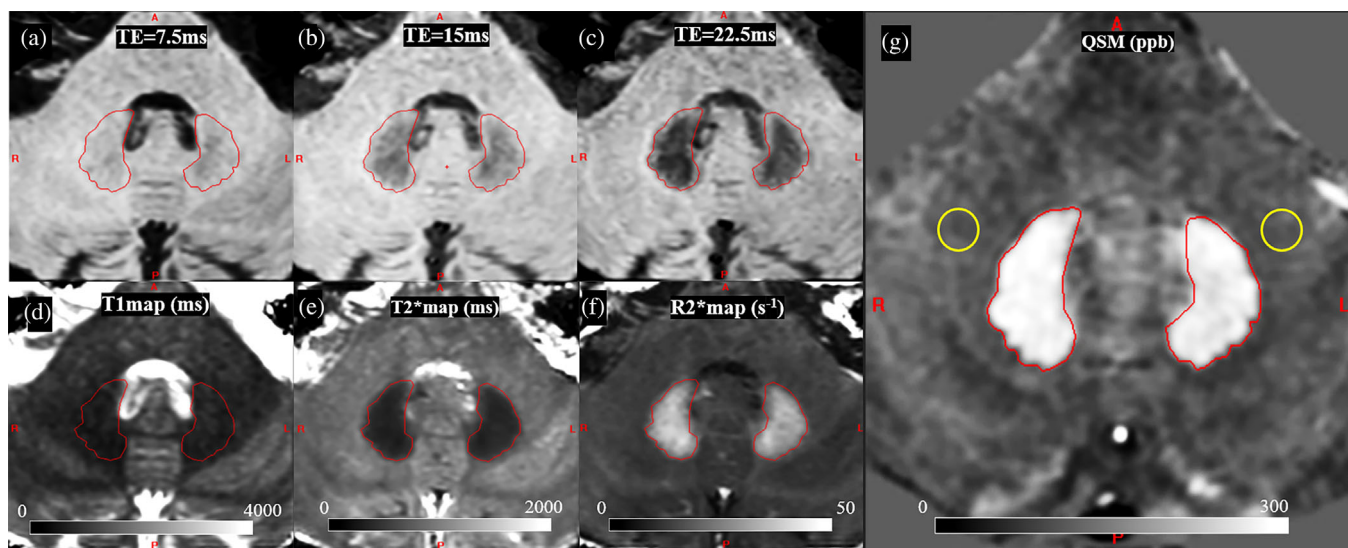


**FIGURE 5** The contrast of the dentate nuclei (DN) with the surrounding white matter (WM). (a–g) show the DN on different modality images with the same slice (a–c): T1 weighted images (T1WI) with three different echo time; (d): T1 map, (e): R2\* map; (f): T2\* map; (g): QSM). The visibility of DN is highest with QSM compared to T1WI, T1 or T2\*/R2\* maps. Red boundaries: DN; yellow boundaries: WM

FN in the TD-PD group was significantly higher than that for the HCs (TD > HCs with  $p = .012$ ) although the difference between the means was small being only  $12.2 \text{ mm}^3$ .

For all participants, the susceptibility increased as a function of volume for the DN and the IN (all  $p < .001$ ) but not the FN ( $p = .74$ ) (Figure 7). The differences in the volume and susceptibility in the DN

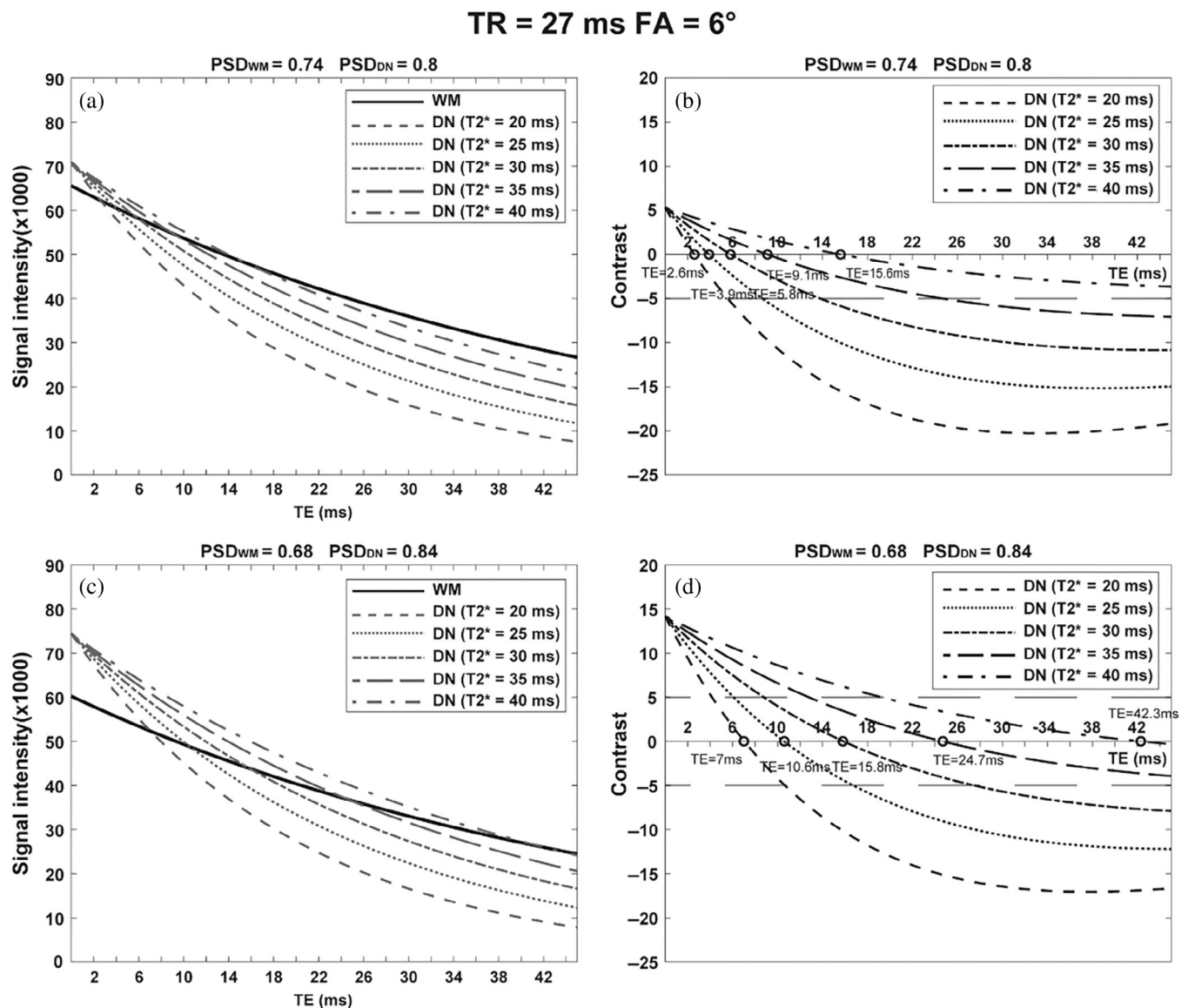


**FIGURE 6** Signal and contrast between the dentate nuclei (DN) and white matter (WM). As a function of echo time (TE) for repetition time (TR) = 27 ms and 6° flip angle. Note the crossover in the contrast, appears at increasing echo times as T2\* of the dentate increases. If the noise in the images is 1 unit, then only the contrast higher than 4:1 or less than -4:1 will be visible in the images. The grey long dashed lines in (b) and (d) indicate a contrast of  $\pm 4:1$  units. (a) and (b) Proton spin density (PSD) of 0.74 for WM and PSD of 0.8 for DN; (c) and (d) PSD of 0.68 for WM and PSD of 0.84 for DN

and IN showed no statistical significance among these four groups (all  $p > .05$ ).

In this work, we investigated the mean volume and susceptibility of the right and left DCN and the mean volume and susceptibility of the bilateral DCN as a function of age in these four groups (see Figures S2–S5). The linear fitting equations for the bilateral DCN volume and mean susceptibility versus age for the HCs are given in Table S3. There were no age-related changes for volume or susceptibility in any of the DCN for any of the four groups; however, there was a tendency for the FN to show a slightly reduced susceptibility as a function of age ( $p = .06$ ) in HCs.

## 4 | DISCUSSION AND CONCLUSIONS

In this study, we made the following observations: (1) all the DCN (DN, IN, and FN) structures, for the most part, could be visualized and delineated in the QSM data; (2) susceptibility increased as a function of volume for both the HC group and disease groups in the DN and the IN but not the FN; (3) the volume of the FN in TD-PD subjects was slightly larger than that for HCs. Other than these findings, there were no differences in volume or susceptibility between the different DCN structures for any of the movement disorder populations (TD-PD, PIGD-TD, and ET) evaluated in this study when compared with



**TABLE 2** The volume and susceptibility (mean value and standard deviations [SDs]) of right and left deep cerebellar nuclei (DCN) in all four groups

	Bonferroni correction										
	HC (n = 80)	ET (n = 39)	PIGD-PD (n = 41)	TD-PD (n = 30)	p-value	HC versus		ET versus		PIGD-PD versus TD-PD	
						HC versus	PIGD-PD	ET versus	PIGD-PD	ET versus	TD-PD
Volume (mm <sup>3</sup> )											
RDN	889.5 ± 214.4	836.2 ± 202.5	863.6 ± 168.4	895.8 ± 173.2	.502	-	-	-	-	-	-
LDN	889.8 ± 214.5	839.4 ± 177.9	881.8 ± 168.5	913.4 ± 166.9	.413	-	-	-	-	.675	-
RIN	44.6 ± 17.9	42.1 ± 17.0	45.6 ± 17.6	46.6 ± 12.0	.704	-	-	-	-	-	-
LIN	45.3 ± 15.3	43.4 ± 18.5	46.1 ± 18.0	48.4 ± 14.9	.653	-	-	-	-	-	-
b-FN	45.9 ± 18.1	49.1 ± 16.8	52.3 ± 18.9	58.1 ± 19.0	.015	-	.408	-	-	.012*	.253
susceptibility (ppb)											
RDN	88.0 ± 24.9	91.2 ± 27.5	93.1 ± 22.8	85.1 ± 19.2	.504	-	-	-	-	-	-
LDN	90.8 ± 24.0	94.5 ± 25.4	95.2 ± 25.4	88.1 ± 21.3	.552	-	-	-	-	-	-
RIN	49.4 ± 19.2	48.2 ± 22.4	56.2 ± 23.3	46.9 ± 19.6	.202	-	.533	-	-	.529	.381
LIN	53.9 ± 20.8	51.1 ± 20.8	58.2 ± 24.0	48.7 ± 18.0	.256	-	-	-	-	.809	.384
b-FN	47.7 ± 22.7	45.5 ± 20.1	42.7 ± 18.2	40.0 ± 16.9	.293	-	-	-	-	.474	-

Abbreviations: b-FN, bilateral fastigial nucleus; ET, Essential tremor; HCs, health controls; LDN, left dentate nucleus; LIN, left interposed nucleus; NA, not available; PIGD, postural instability/gait difficulty; PD, RDN, right dentate nucleus; RIN, right interposed nucleus; TD-PD, tremor dominant PD.

\*p values < .05 were considered significant.

HCs. Our measurements, as a whole, provide standardization for susceptibility and volume for the DCN structures.

In this work, we took advantage of QSM to better visualize each component of the DCN. Previous studies such as Dimitrova et al. (2002) used a single brain dataset to create an MRI atlas of the DCN with a T1W fast low-angle shot sequence at 1.5 T with TR/TE = 80/50 ms and a FA = 10°. These long TEs and TRs led to a low signal-to-noise ratio (SNR) and so they acquired the data five times. Additionally, Deoni and Catani (2007) used T1 and PSD maps with imaging parameters: resolution = 0.9 × 0.9 × 1 mm<sup>3</sup>, TR/TE = 7.2 ms/1.6 ms, FA = 4°, and 18° at 3 T MR, as well as a resolution = 0.7 × 0.7 × 0.7 mm<sup>3</sup> and similar TR/TE and FA at 7 T to differentiate the DCN. Nonetheless, the DCN contrast on these T1 and PSD maps was poor. The DN is one of the DGM structures with the most abundant iron which leads to a reduction in both its T1 and T2\*; hence, the DN begins to look like WM and disappears in most short TE images. Using the tissue properties for spin density, T1 and T2\*, we showed the lack of contrast for the DN for short TR imaging relative to the surrounding WM as expected (Figure 5). This predicted lack of contrast explains why T1W images do a poor job in visualizing the DN. Note that with an SNR as high as 30:1 and a signal of 60 units that the noise would be 2 units. Therefore, one would need a contrast of at least 4–6 units (two to three standard deviations) to differentiate the border of the DN with the surrounding tissue which for a T2\* = 25 ms would require imaging with a TE near 15 ms (Figure 6).

Diedrichsen et al. (2011) acquired SWI at 7 T with a resolution = 0.5 × 0.5 × 0.5 mm<sup>3</sup>, TR/TE = 35/16.9 ms, FA = 19°, and a total scan time = 16 min, 14 s; a rather long scanning time. If the same method were run at 3T, the TE would increase to 40 ms and the TR to 55 ms making the total acquisition time equal to 25 min, 30 s. In contrast, we applied two FAs each with multiple echoes to collect reasonably high-resolution QSM data in just 9 min. This shorter acquisition time is more realistic clinically especially when imaging patients with movement disorders. Additionally, unlike R2\* which is susceptible to field inhomogeneities and the dipole fields for structures with high iron content, QSM phase processing eliminates these influences and the results are not orientation dependent. More importantly, QSM has the distinct advantage that susceptibility is not dependent on the tissue properties such as spin density, T1 or T2\* values, or the imaging parameters such as main field strength, TE, or FA (however, SNR in the QSM data does depend on SNR in the phase data and, in this sense, QSM results have a dependence on the echo time) (Haacke et al., 2015). Although the reconstruction algorithms for QSM are sophisticated and involve many steps, several studies have shown that the results are highly reproducible even at different field strengths, different resolutions and for different vendors scanners (Deh et al., 2015; Hinoda et al., 2015; Li et al., 2020). Our results show that, in terms of visualizing the DCN, the optimal approach is to use QSM data rather than T1W, T2\* W, R2\*, T1, PSD, or SWI. Nevertheless, weighing the importance of good CNR and SNR and total scan time at 3T, the DCN can be seen reasonably well with a TE of 22.5 ms.

In the present study, the results for the volume in HCs (right DN: 889.5 ± 214.4 mm<sup>3</sup>, left DN: 889.8 ± 214.5 mm<sup>3</sup>) were in agreement

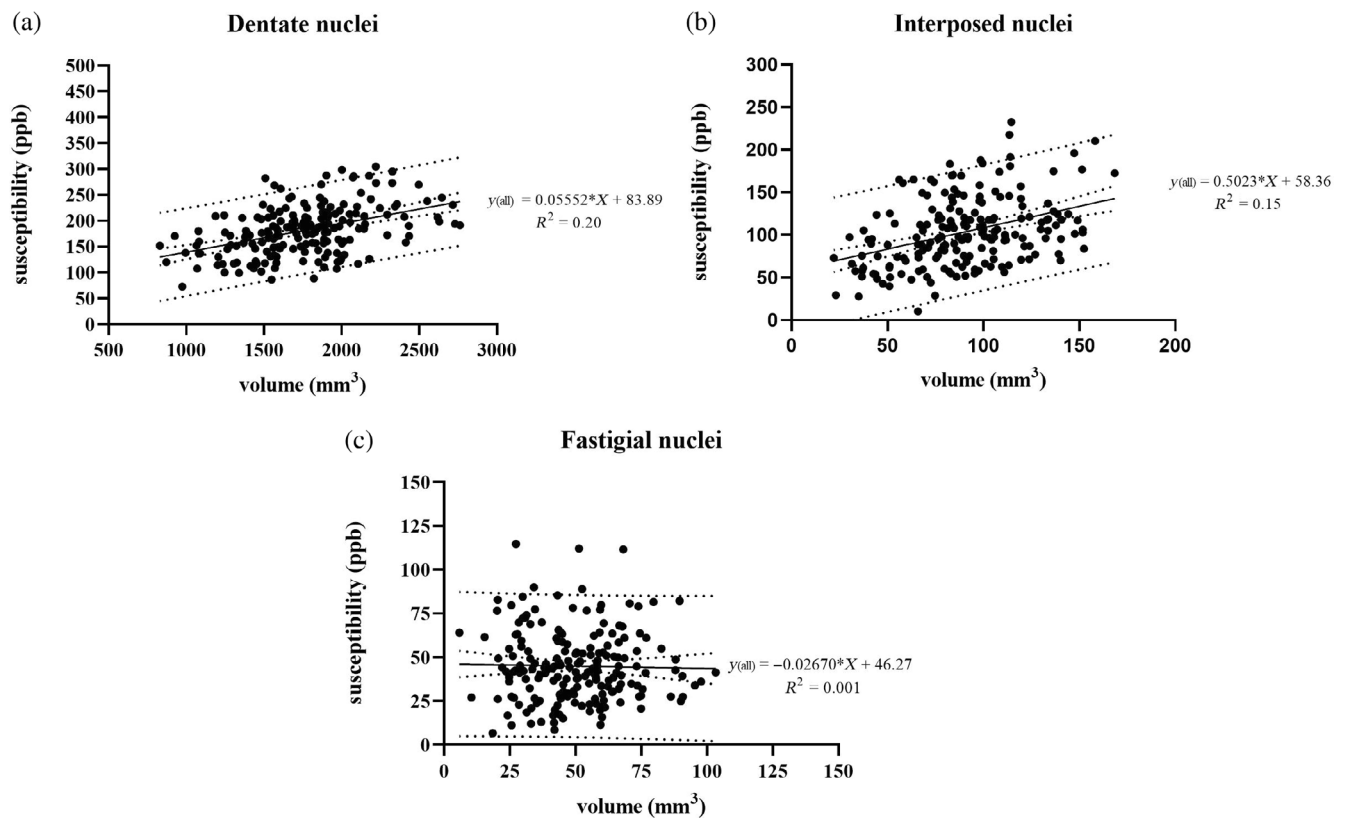


**FIGURE 7** Plots of susceptibility versus volume for the addition of left and right sides in all subjects ( $n = 190$ ). In the dentate nuclei (DN) and interposed nuclei (IN), the susceptibility was positively correlated with the volume, but not in fastigial nuclei (FN). (a) DN susceptibility versus volume (with  $y = 0.05552 * X + 83.89$ ,  $R^2 = 0.20$ ,  $p < .001$ ); (b) IN susceptibility versus volume (with  $y = 0.5023 * X + 58.36$ ,  $R^2 = 0.15$ ,  $p < .000$ ) and (c) FN susceptibility versus volume (with  $y = -0.02670 * X + 46.27$ ,  $R^2 = 0.001$ ,  $p = .74$ )

with the results of several other studies (Deoni & Catani, 2007, Dimitrova et al., 2006, He, Huang, et al., 2017, Li et al., 2019, Ward et al., 2019). But the results were higher than those of another work (He, Langley, et al., 2017), in that paper, a thresholding approach was used to segment DN leading to a smaller estimate of the DN volume. Several other studies showed even lower estimates of the DN volume. The imaging results for the volumes of the DCN conducted by Diedrichsen et al. (right DN:  $366.1 \pm 85.2 \text{ mm}^3$ , left DN:  $362.8 \pm 89.2 \text{ mm}^3$ ) (Diedrichsen et al., 2011) and the histological results reported by Tellmann et al. (right DN:  $394.5 \pm 94.5 \text{ mm}^3$ , left DN:  $390.2 \pm 99.3 \text{ mm}^3$ ) (Tellmann et al., 2015) showed less than half the values reported here. For MR results, the reason may be that the contrast in the QSM data is very high making it easier to demarcate the boundaries while Diedrichsen et al. marked the ROIs on the phase images and refined them on the SWI images. In the histological study of Tellmann et al., the shrinkage of the cell body following the dehydration processing of the postmortem brain could lead to an underestimate of the volume of the DCN. Also, the silver staining (Merker, 1983) used in their study did not reach the limit of selectively impregnating the tissue. However, for small structures, particularly the FN (with a diameter of roughly 3 mm [Diedrichsen et al., 2011; Dimitrova et al., 2002]) there can be significant partial volume errors. If there exist not  $< 4$  pixels across the object (4 pixels with a resolution

of 0.67 mm), partial volume effects can be large. In practice, the high iron content can cause the ROIs to be drawn slightly larger than the true boundary. But this bias will be present for all the structures and will decrease as the size of the structure increases. Although the resolution in other studies was higher than 1 mm (0.5 mm isotropic for Diedrichsen et al.'s study and 20  $\mu\text{m}$  in-plane resolution for the sectioned images), the visibility of the structures was not determined by QSM and so contrast issues may have played an important role in underestimating the total volume of these structures. Most of the higher volume results including the current results in this paper were obtained from QSM or QSM/T1 data with a manual or automatic approach, except for Dimitrova et al. and Deoni SC et al. who used T2\*W and quantitative T1/proton density imaging, respectively. The reason for the wide discrepancy in the volume estimates among the existing studies could be related to both the visibility and varying imaging parameters, as well as analysis methods. More studies would be useful to explore the reasons behind the imaging and histological differences. In line with previous results (Diedrichsen et al., 2011; He, Langley, et al., 2017; Tellmann et al., 2015; Ward et al., 2019), there was no difference in the left and right side DN and IN volumes, whereas, Deoni et al. (Deoni & Catani, 2007) found that the volumes of the bilateral DN were different, but they only evaluated a small number of subjects.

Our findings of the mean susceptibility for the DN in HCs (right DN:  $88.0 \pm 24.9$  ppb, left DN:  $90.8 \pm 24.0$  ppb) agreed well with those in other studies (Shin et al., 2018; Ward et al., 2019). However, the DN susceptibility value was slightly higher than in other studies (He, Huang, et al., 2017; Kim et al., 2021; Persson et al., 2015), which could be because we used a higher resolution ( $0.67 \times 0.67 \times 1.34$  mm<sup>3</sup>) which makes it easier to accurately draw the boundary of the DN (where the capsule is quite clear because of its high iron content). Moreover, similar to the volume of the left and right DN and IN, good consistency was also seen in the susceptibility values of the left and right DN and IN (Figure S6).

Regarding the correlation between volume and susceptibility, we found that susceptibility increased as a function of volume for the DN and the IN but not the FN. It is well-known that iron plays a key role in many neurological diseases (Ward et al., 2014). Whether the increased iron is pathogenic or just a part of normal aging is still unclear. Increased iron deposition with larger DCN structures is a novel finding and could represent normal or pathophysiologic processes. Therefore, it is appropriate to evaluate the relationship between volume and susceptibility in normal individuals. Some diseases, such as Friedreich's ataxia show the opposite phenomenon, that is, increased iron deposition of the DN is accompanied by severe atrophy of the nuclei, especially in the early disease course (Ward et al., 2019). Our results can be seen as providing normative reference values for susceptibility and volume and can be used in studying other diseases, and to our knowledge, this is the first time that an association between the susceptibility and volume of the DCN has been found.

In this study, the volume of the FN in the TD-PD group was significantly higher than that for the HCs (TD > HCs with  $p = .012$ ). Despite the fact that the difference between the means was small, being only 12.2 mm<sup>3</sup>, this still represents an increase in the volume of roughly 24%. Although using a threshold of change is somewhat arbitrary, one might consider a change in volume or susceptibility of >10% meaningful. Therefore, these changes may have some physiologic importance. Except for that, we did not find any differences in the DCN volume and susceptibility values among the HCs, ET, and subtypes of PD. Previous research has been unable to reach a consensus on the issue of volume and iron deposition in the DCN in movement disorders. A postmortem study substantiated that the neuronal density and total neuronal number do not differ between ET cases and controls (Hartstone et al., 2021), but at the same time another study also concluded that there was no evidence to show an iron deposition difference in the DN among HCs, PD, and ET patients (Pietracupa et al., 2021). Although the whole brain voxel-based analysis showed a significant difference of T2\* in the right DN, the difference did not survive family-wise error correction for multiple comparisons ( $p > .05$ ) (Novellino et al., 2013). In ET and HCs, the number of neurons and neuronal density did not differ but neuronal loss occurred in Purkinje cells (Hartstone et al., 2021). Also, compared with HCs and PD, defective GABA receptors have been reported in ET (Paris-Robidas et al., 2012). Our results indirectly support the hypothesis that the source of dysfunction in ET is associated with the

microstructure changes in the cerebellum rather than the neuronal number or the volume of the DCN (Louis et al., 2014; Zhang & Santaniello, 2019). Pietracupa et al. have also suggested that the neuronal loss and subsequent brain iron deposition in the subcortical nuclei may not be pathological hallmarks of ET (Pietracupa et al., 2021). Even though the cerebello-thalamo-cortical circuit is involved in tremor, the role of neuronal number and increased iron deposition in the DN in the pathophysiological mechanism of tremor still needs further investigation.

In addition, the findings of PD subtype groups in the present study were divergent from our expectations. The results from previous studies were also varied. He, Huang, et al. (2017) measured the DN volume while investigating DN iron deposition in HCs and PD patients and they noted that there was no significant difference between the DN volumes of HCs and TD-PD and akinetic rigidity dominant PD patients. This was consistent with our results, but He et al. demonstrated that the DN iron content could be a potential biomarker to differentiate TD-PD from other subtypes. In the same year, Guan, Xuan, Gu, Xu, et al. (2017) also showed that excessive iron deposition in the DN was seen only in TD-PD patients; while using R2\* as a measure, neither study found a difference in PD subtypes. Moreover, a recent paper (Chen et al., 2020) focused on DN iron deposition in HCs, TD-PD, and PIGD-PD and came to the same conclusions as He et al. and Guan et al. Nonetheless when considering PD patients as a whole group, some studies failed to find any DN iron content changes in HCs and PD patients (Guan, Xuan, Gu, Huang, et al., 2017; Shin et al., 2018), and two papers reported that compared to HCs, the susceptibility value in the DN showed a decreased trend (Kim et al., 2021) or significantly decreased (Acosta-Cabronero et al., 2017) in PD. Several possible reasons could explain differing results between studies: first, some studies may not have considered other concurrent diseases of participants. Specifically, there has been a study finding the susceptibility of the DN decreases in individuals with hypertension while it increases in individuals with a history of type 2 diabetes mellitus (Li et al., 2021). Also, the choice of imaging parameters such as the slice thickness could lead to changes in volume measurements. Therefore, future studies should rigorously formulate inclusion criteria to avoid the presence of confounding diseases and should have high enough resolution to ensure good volume estimates.

In line with previous papers (Bilgic et al., 2012; Li et al., 2015; Persson et al., 2015), there were no age-related changes in the DN susceptibility in HCs. Conversely, several studies found a linear or nonlinear age-related increase in susceptibility for DN (Burgetova et al., 2021; Li et al., 2014, 2020). The distribution of age of subjects could explain that discrepancy, the age of our participants ranged from 43 to 80 years while a previous study (Maschke et al., 2004) demonstrated that age-related changes in DN iron deposition mostly occurred between the ages of 20 and 40 years and to a lesser degree after 40 years. Meanwhile, Persson et al. stated in their research that age only explained 4% of the variance in DN mean susceptibility (Persson et al., 2015). Additionally, there were several structures with significant differences between men and women (Table S4), but the

changes in the volume and susceptibility showed the opposite tendency, especially for FN which in the female has a higher volume but with a lower susceptibility value. Specifically, the susceptibility was 22 ppb higher for men. This phenomenon could be related to sex hormones. There have been studies suggesting that estrogen may act as an antioxidant that could moderate iron accumulation (Grubić Kezele & Ćurko-Cofek, 2020; Shin et al., 2020). Furthermore, premenopausal iron loss through menstruation (Tishler et al., 2012) and modest postmenopausal iron accumulation may also play an important role in these differences. However, if there is a systematic bias leading to an increase in volume that could reduce the mean susceptibilities, using an automated program such as dynamic programming would likely show a decreased volume and a concomitant increase in susceptibility. Even in this situation, the differences in susceptibility will likely remain the same.

Although the volume and susceptibility of the DCN showed no obvious differences among the HCs, ET, and subtypes of PD in this study, the DN susceptibility and volume measurements are crucial to other cerebellar-related diseases. QSM would be a potent tool to monitor the progression of Friedreich's Ataxia (Ward et al., 2019) and has the potential to discriminate between multiple system atrophy and cerebellar ataxia (Sugiyama et al., 2019). Meanwhile, the superb ability of QSM to visualize the DGM will help to target the DCN in surgical operations such as deep brain stimulation (Deistung et al., 2013; Paraguay et al., 2021). For the IN and FN, there have been no publications assessing their iron deposition, let alone investigations concerning differences in the four groups. One major benefit of this study was that the volume and susceptibility values of the IN and FN have been tabulated as a function of age for older individuals. These values can be used as a reference in future movement disorder studies when evaluating iron accumulation and volume of the DCN.

There are several limitations to this work. First, the sample size is relatively small for each movement disorder group, and because of the small sample size, we did not include the indeterminate group of PD. Second, the age range was only from 43 to 80 years; no DCN volume or susceptibility baseline for younger individuals was provided. Finally, although we analyzed the maximum susceptibility values of the DCN in these four groups, we did not apply the method of measuring susceptibility value on QSM referred to as region II analysis which is a means to find those pixels that have higher than two standard deviations above the mean of the structure of interest (Liu et al., 2016). In many of the DGM, there is a bimodal distribution of lower and higher susceptibility values. Region II results have proven to be a more sensitive approach for monitoring age-dependent changes in iron content compared to the global analysis (Li et al., 2020; Liu et al., 2016). However, we did evaluate the maximum susceptibility values in all structures and came to the same conclusion that there were no significant differences between any measures and the four different groups in this study (Table S5) and no obvious age-related trends (Figure S7). Region II analysis may be quite interesting since the capsule of the DN can often have higher iron than the interior especially since some research has already reported the distribution of iron in DN is uneven (He, Langley, et al., 2017). Therefore,

further investigations regarding the specific distribution of iron in the DN are warranted, especially in cerebellar-related diseases. Additionally, if there are enough patients, it is worth investigating the DCN volume and susceptibility of the PD indeterminate group.

In summary, QSM provides a clear means to visualize the DCN and quantify their iron content while STAGE provides a means to quantify their tissue properties. In this study, the DCN volume and susceptibility could not differentiate between PD subtypes and ET patients, but the results for the volume and susceptibility of the DCN can be used as a reference in future studies of movement disorders.

## AUTHOR CONTRIBUTIONS

**Youmin Zhang:** Writing – Original draft; Data curation; Investigation; Formal analysis; Funding acquisition. **Pei Huang:** Writing – Review & Editing; Data curation; Investigation. **Xinhui Wang:** Writing – Review & Editing; Data curation; Investigation; Formal analysis. **Qiuyun Xu:** Writing – original draft; Methodology; Formal analysis. **Yu Liu:** Writing – Review & Editing; Resources; Investigation. **Zhijia Jin:** Writing – Review & Editing; Investigation. **Yan Li:** Writing – Review & Editing; Investigation. **Zenghui Cheng:** Writing – Review & Editing; Resources; Investigation. **Rongbiao Tang:** Writing – Review & Editing; Resources; Investigation. **Shengdi Chen:** Conceptualization; Funding acquisition; Project administration; Investigation; Resources. **Naying He:** Conceptualization; Supervision; Funding acquisition; Resources; Writing – Review & Editing. **Fuhua Yan:** Conceptualization; Supervision; Funding acquisition; Resources; Writing – Review & Editing. **E. Mark Haacke:** Conceptualization; Writing – original draft; Supervision; Methodology.

## ACKNOWLEDGMENTS

This work was supported in part by the National Natural Science Foundation of China (grant number: 81971576 for Fuhua Yan, M.D., Naying He, M.D.), National Key R&D Program of China (2022YFC2009905/2022YFC2009900) and the Innovative Research Team of High-level Local Universities in Shanghai.

## CONFLICT OF INTEREST

The authors declare no potential conflicts of interest.

## DATA AVAILABILITY STATEMENT

The source and collection of the data in this paper have been described in the Methods section. The data are available upon a reasonable request with a formal data sharing agreement from the corresponding author.

## ETHICS STATEMENT

This study was approved by the local ethics committee.

## PATIENT CONSENT STATEMENT

All subjects signed a consent form.

## ORCID

Fuhua Yan  <https://orcid.org/0000-0002-5910-1506>

## REFERENCES

- Abbas, Z., Gras, V., Möllenhoff, K., Oros-Peusquens, A. M., & Shah, N. J. (2015). Quantitative water content mapping at clinically relevant field strengths: A comparative study at 1.5 T and 3 T. *NeuroImage*, 106, 404–413. <https://doi.org/10.1016/j.neuroimage.2014.11.017>
- Acosta-Cabronero, J., Betts, M. J., Cardenas-Blanco, A., Yang, S., & Nestor, P. J. (2016). In vivo MRI mapping of brain iron deposition across the adult lifespan. *The Journal of Neuroscience*, 36(2), 364–374. <https://doi.org/10.1523/JNEUROSCI.1907-15.2016>
- Acosta-Cabronero, J., Cardenas-Blanco, A., Betts, M. J., Butryn, M., Valdes-Herrera, J. P., Galazky, I., & Nestor, P. J. (2017). The whole-brain pattern of magnetic susceptibility perturbations in Parkinson's disease. *Brain*, 140(1), 118–131. <https://doi.org/10.1093/brain/aww278>
- Aoki, S., Okada, Y., Nishimura, K., Barkovich, A. J., Kjos, B. O., Brasch, R. C., & Norman, D. (1989). Normal deposition of brain iron in childhood and adolescence: MR imaging at 1.5 T. *Radiology*, 172(2), 381–385. <https://doi.org/10.1148/radiology.172.2.2748819>
- Barbosa, J. H., Santos, A. C., Tumas, V., Liu, M., Zheng, W., Haacke, E. M., & Salmon, C. E. (2015). Quantifying brain iron deposition in patients with Parkinson's disease using quantitative susceptibility mapping, R2 and R2\*. *Magnetic Resonance Imaging*, 33(5), 559–565. <https://doi.org/10.1016/j.mri.2015.02.021>
- Bhatia, K. P., Bain, P., Bajaj, N., Elble, R. J., Hallett, M., Louis, E. D., Raethjen, J., Stamelou, M., Testa, C. M., Deuschl, G., & Tremor Task Force of the International Parkinson and Movement Disorder Society. (2018). Consensus statement on the classification of tremors. From the task force on tremor of the International Parkinson and Movement Disorder Society. *Movement Disorders*, 33(1), 75–87. <https://doi.org/10.1002/mds.27121>
- Bilgic, B., Pfefferbaum, A., Rohlfing, T., Sullivan, E. V., & Adalsteinsson, E. (2012). MRI estimates of brain iron concentration in normal aging using quantitative susceptibility mapping. *NeuroImage*, 59(3), 2625–2635. <https://doi.org/10.1016/j.neuroimage.2011.08.077>
- Burgetova, R., Dusek, P., Burgetova, A., Pudlac, A., Vaneckova, M., Horakova, D., Krasensky, J., Varga, Z., & Lambert, L. (2021). Age-related magnetic susceptibility changes in deep grey matter and cerebral cortex of normal young and middle-aged adults depicted by whole brain analysis. *Quantitative Imaging in Medicine and Surgery*, 11(9), 3906–3919. <https://doi.org/10.21037/qims-21-87>
- Chai, C., Yan, S., Chu, Z., Wang, T., Wang, L., Zhang, M., Zuo, C., Haacke, E. M., Xia, S., & Shen, W. (2015). Quantitative measurement of brain iron deposition in patients with haemodialysis using susceptibility mapping. *Metabolic Brain Disease*, 30(2), 563–571. <https://doi.org/10.1007/s11011-014-9608-2>
- Chen, J., Cai, T., Li, Y., Chi, J., Rong, S., He, C., Li, X., Zhang, P., Wang, L., & Zhang, Y. (2020). Different iron deposition patterns in Parkinson's disease subtypes: A quantitative susceptibility mapping study. *Quantitative Imaging in Medicine and Surgery*, 10(11), 2168–2176. <https://doi.org/10.21037/qims-20-285>
- Chen, Y., Liu, S., Wang, Y., Kang, Y., & Haacke, E. M. (2018). STrategically acquired gradient Echo (STAGE) imaging, part I: Creating enhanced T1 contrast and standardized susceptibility weighted imaging and quantitative susceptibility mapping. *Magnetic Resonance Imaging*, 46, 130–139. <https://doi.org/10.1016/j.mri.2017.10.005>
- Deh, K., Nguyen, T. D., Eskreis-Winkler, S., Prince, M. R., Spincemaille, P., Gauthier, S., Kovanlikaya, I., Zhang, Y., & Wang, Y. (2015). Reproducibility of quantitative susceptibility mapping in the brain at two field strengths from two vendors. *Journal of Magnetic Resonance Imaging*, 42(6), 1592–1600. <https://doi.org/10.1002/jmri.24943>
- Deistung, A., Schafer, A., Schweser, F., Biedermann, U., Turner, R., & Reichenbach, J. R. (2013). Toward in vivo histology: A comparison of quantitative susceptibility mapping (QSM) with magnitude-, phase-, and R2\*-imaging at ultra-high magnetic field strength. *NeuroImage*, 65, 299–314. <https://doi.org/10.1016/j.neuroimage.2012.09.055>
- Deistung, A., Schweser, F., & Reichenbach, J. R. (2017). Overview of quantitative susceptibility mapping. *NMR in Biomedicine*, 30(4), e3569. <https://doi.org/10.1002/nbm.3569>
- Deistung, A., Stefanescu, M. R., Ernst, T. M., Schlamann, M., Ladd, M. E., Reichenbach, J. R., & Timmann, D. (2016). Structural and functional magnetic resonance imaging of the cerebellum: Considerations for assessing cerebellar ataxias. *Cerebellum*, 15(1), 21–25. <https://doi.org/10.1007/s12311-015-0738-9>
- Deoni, S. C., & Catani, M. (2007). Visualization of the deep cerebellar nuclei using quantitative T1 and rho magnetic resonance imaging at 3 tesla. *NeuroImage*, 37(4), 1260–1266. <https://doi.org/10.1016/j.neuroimage.2007.06.036>
- Diedrichsen, J., Maderwald, S., Küper, M., Thürling, M., Rabe, K., Gizewski, E. R., Ladd, M. E., & Timmann, D. (2011). Imaging the deep cerebellar nuclei: A probabilistic atlas and normalization procedure. *NeuroImage*, 54(3), 1786–1794. <https://doi.org/10.1016/j.neuroimage.2010.10.035>
- Dieringer, M. A., Deimling, M., Santoro, D., Wuerfel, J., Madai, V. I., Sobesky, J., von Knobelsdorff-Brenkenhoff, F., Schulz-Menger, J., & Niendorf, T. (2014). Rapid parametric mapping of the longitudinal relaxation time T1 using two-dimensional variable flip angle magnetic resonance imaging at 1.5 tesla, 3 tesla, and 7 tesla. *PLoS One*, 9(3), e91318. <https://doi.org/10.1371/journal.pone.0091318>
- Dimitrova, A., Weber, J., Redies, C., Kindsvater, K., Maschke, M., Kolb, F. P., Forsting, M., Diener, H. C., & Timmann, D. (2002). MRI atlas of the human cerebellar nuclei. *NeuroImage*, 17(1), 240–255. <https://doi.org/10.1006/nimg.2002.1124>
- Dimitrova, A., Zeljko, D., Schwarze, F., Maschke, M., Gerwig, M., Frings, M., Beck, A., Aurich, V., Forsting, M., & Timmann, D. (2006). Probabilistic 3D MRI atlas of the human cerebellar dentate/interposed nuclei. *NeuroImage*, 30(1), 12–25. <https://doi.org/10.1016/j.neuroimage.2005.09.020>
- du, G., Liu, T., Lewis, M. M., Kong, L., Wang, Y., Connor, J., Mailman, R. B., & Huang, X. (2016). Quantitative susceptibility mapping of the midbrain in Parkinson's disease. *Movement Disorders*, 31(3), 317–324. <https://doi.org/10.1002/mds.26417>
- Grubić Kezele, T., & Ćurko-Cofek, B. (2020). Age-related changes and sex-related differences in brain iron metabolism. *Nutrients*, 12(9), 2601. <https://doi.org/10.3390/nu12092601>
- Guan, X., Xuan, M., Gu, Q., Huang, P., Liu, C., Wang, N., Xu, X., Luo, W., & Zhang, M. (2017). Regionally progressive accumulation of iron in Parkinson's disease as measured by quantitative susceptibility mapping. *NMR in Biomedicine*, 30(4), e3489. <https://doi.org/10.1002/nbm.3489>
- Guan, X., Xuan, M., Gu, Q., Xu, X., Huang, P., Wang, N., Shen, Z., Xu, J., Luo, W., & Zhang, M. (2017). Influence of regional iron on the motor impairments of Parkinson's disease: A quantitative susceptibility mapping study. *Journal of Magnetic Resonance Imaging*, 45(5), 1335–1342. <https://doi.org/10.1002/jmri.25434>
- Haacke, E. M., Chen, Y., Utraiainen, D., Wu, B., Wang, Y., Xia, S., He, N., Zhang, C., Wang, X., Lagana, M. M., Luo, Y., Fatemi, A., Liu, S., Gharabaghi, S., Wu, D., Sethi, S. K., Huang, F., Sun, T., Qu, F., ... Yan, F. (2020). STrategically acquired gradient Echo (STAGE) imaging, part III: Technical advances and clinical applications of a rapid multi-contrast multi-parametric brain imaging method. *Magnetic Resonance Imaging*, 65, 15–26. <https://doi.org/10.1016/j.mri.2019.09.006>
- Haacke, E. M., Liu, S., Buch, S., Zheng, W., Wu, D., & Ye, Y. (2015). Quantitative susceptibility mapping: Current status and future directions. *Magnetic Resonance Imaging*, 33(1), 1–25. <https://doi.org/10.1016/j.mri.2014.09.004>
- Hallgren, B., & Sourander, P. (1958). The effect of age on the non-haem iron in the human brain. *Journal of Neurochemistry*, 3(1), 41–51. <https://doi.org/10.1111/j.1471-4159.1958.tb12607.x>
- Hartstone, W. G., Brown, M. H., Kelly, G. C., Tate, W. J., Kuo, S. H., Dwork, A. J., Louis, E. D., & Faust, P. L. (2021). Dentate nucleus neuronal density: A postmortem study of essential tremor versus control

- brains. *Movement Disorders*, 36(4), 995–999. <https://doi.org/10.1002/mds.28402>
- He, N., Huang, P., Ling, H., Langley, J., Liu, C., Ding, B., Huang, J., Xu, H., Zhang, Y., Zhang, Z., Hu, X., Chen, S., & Yan, F. (2017). Dentate nucleus iron deposition is a potential biomarker for tremor-dominant Parkinson's disease. *NMR in Biomedicine*, 30(4), e3554. <https://doi.org/10.1002/nbm.3554>
- He, N., Langley, J., Huddleston, D. E., Ling, H., Xu, H., Liu, C., Yan, F., & Hu, X. P. (2017). Improved neuroimaging atlas of the dentate nucleus. *Cerebellum*, 16(5–6), 951–956. <https://doi.org/10.1007/s12311-017-0872-7>
- Helmich, R. C., Hallett, M., Deuschl, G., Toni, I., & Bloem, B. R. (2012). Cerebral causes and consequences of parkinsonian resting tremor: A tale of two circuits? *Brain*, 135(Pt 11), 3206–3226. <https://doi.org/10.1093/brain/aww023>
- Hinoda, T., Fushimi, Y., Okada, T., Fujimoto, K., Liu, C., Yamamoto, A., Okada, T., Kido, A., & Togashi, K. (2015). Quantitative susceptibility mapping at 3 T and 1.5 T: Evaluation of consistency and reproducibility. *Investigative Radiology*, 50(8), 522–530.
- Ibrahim, M. F., Beevis, J. C., & Empson, R. M. (2021). Essential Tremor - A Cerebellar Driven Disorder? *Neuroscience*, 462, 262–273. <https://doi.org/10.1016/j.neuroscience.2020.11.002>
- Kakita, A., Takahashi, H., Homma, Y., & Ikuta, F. (1994). Lewy bodies in the cerebellar dentate nucleus of a patient with Parkinson's disease. *Pathology International*, 44(12), 878–880. <https://doi.org/10.1111/j.1440-1827.1994.tb01688.x>
- Kim, M., Yoo, S., Kim, D., Cho, J. W., Kim, J. S., Ahn, J. H., Mun, J. K., Choi, I., Lee, S. K., & Youn, J. (2021). Extra-basal ganglia iron content and non-motor symptoms in drug-naïve, early Parkinson's disease. *Neurological Sciences*, 42(12), 5297–5304. <https://doi.org/10.1007/s10072-021-05223-0>
- Koeppen, A. H., Michael, S. C., Knutson, M. D., Haile, D. J., Qian, J., Levi, S., Santambrogio, P., Garrick, M. D., & Lamarche, J. B. (2007). The dentate nucleus in Friedreich's ataxia: The role of iron-responsive proteins. *Acta Neuropathologica*, 114(2), 163–173. <https://doi.org/10.1007/s00401-007-0220-y>
- Langkammer, C., Schweser, F., Krebs, N., Deistung, A., Goessler, W., Scheurer, E., Sommer, K., Reishofer, G., Yen, K., Fazekas, F., Ropele, S., & Reichenbach, J. R. (2012). Quantitative susceptibility mapping (QSM) as a means to measure brain iron? A post mortem validation study. *Neuroimage*, 62(3), 1593–1599. <https://doi.org/10.1016/j.neuroimage.2012.05.049>
- Li, J., Zhang, Q., Che, Y., Zhang, N., & Guo, L. (2021). Iron deposition characteristics of deep gray matter in elderly individuals in the community revealed by quantitative susceptibility mapping and multiple factor analysis. *Frontiers in Aging Neuroscience*, 13, 611891. <https://doi.org/10.3389/fnagi.2021.611891>
- Li, W., Langkammer, C., Chou, Y. H., Petrovic, K., Schmidt, R., Song, A. W., Madden, D. J., Ropele, S., & Liu, C. (2015). Association between increased magnetic susceptibility of deep gray matter nuclei and decreased motor function in healthy adults. *NeuroImage*, 105, 45–52. <https://doi.org/10.1016/j.neuroimage.2014.10.009>
- Li, W., Wu, B., Batrachenko, A., Bancroft-Wu, V., Morey, R. A., Shashi, V., Langkammer, C., de Bellis, M. D., Ropele, S., Song, A. W., & Liu, C. (2014). Differential developmental trajectories of magnetic susceptibility in human brain gray and white matter over the lifespan. *Human Brain Mapping*, 35(6), 2698–2713. <https://doi.org/10.1002/hbm.22360>
- Li, X., Chen, L., Kuttan, K., Ceritoglu, C., Li, Y., Kang, N., Hsu, J. T., Qiao, Y., Wei, H., Liu, C., Miller, M. I., Mori, S., Yousem, D. M., van Zijl, P. C. M., & Faria, A. V. (2019). Multi-atlas tool for automated segmentation of brain gray matter nuclei and quantification of their magnetic susceptibility. *NeuroImage*, 191, 337–349. <https://doi.org/10.1016/j.neuroimage.2019.02.016>
- Li, Y., Sethi, S. K., Zhang, C., Miao, Y., Yerramsetty, K. K., Palutla, V. K., Gharabaghi, S., Wang, C., He, N., Cheng, J., Yan, F., & Haacke, E. M. (2020). Iron content in deep gray matter as a function of age using quantitative susceptibility mapping: A multicenter study. *Frontiers in Neuroscience*, 14, 607705. <https://doi.org/10.3389/fnins.2020.607705>
- Lim, S.-Y., Tan, A. H., Ahmad-Annuar, A., Klein, C., Tan, L. C. S., Rosales, R. L., Bhidayasiri, R., Wu, Y. R., Shang, H. F., Evans, A. H., Pal, P. K., Hattori, N., Tan, C. T., Jeon, B., Tan, E. K., & Lang, A. E. (2019). Parkinson's disease in the Western Pacific region. *The Lancet Neurology*, 18(9), 865–879. [https://doi.org/10.1016/s1474-4422\(19\)30195-4](https://doi.org/10.1016/s1474-4422(19)30195-4)
- Liu, M., Liu, S., Ghassaban, K., Zheng, W., Diccio, D., Miao, Y., Habib, C., Jazmati, T., & Haacke, E. M. (2016). Assessing global and regional iron content in deep gray matter as a function of age using susceptibility mapping. *Journal of Magnetic Resonance Imaging*, 44(1), 59–71. <https://doi.org/10.1002/jmri.25130>
- Louis, E. D., & Ferreira, J. J. (2010). How common is the most common adult movement disorder? Update on the worldwide prevalence of essential tremor. *Movement Disorders*, 25(5), 534–541. <https://doi.org/10.1002/mds.22838>
- Louis, E. D., Lee, M., Babij, R., Ma, K., Cortes, E., Vonsattel, J. P., & Faust, P. L. (2014). Reduced Purkinje cell dendritic arborization and loss of dendritic spines in essential tremor. *Brain*, 137(Pt 12), 3142–3148. <https://doi.org/10.1093/brain/awu314>
- Manto, M., & Oulad Ben Taib, N. (2010). Cerebellar nuclei: Key roles for strategically located structures. *Cerebellum*, 9(1), 17–21. <https://doi.org/10.1007/s12311-010-0159-8>
- Maschke, M., Weber, J., Dimitrova, A., Bonnet, U., Bohrenkämper, J., Sturm, S., Kindsvater, K., Müller, B. W., Gastpar, M., Diener, H. C., Forsting, M., & Timmann, D. (2004). Age-related changes of the dentate nuclei in normal adults as revealed by 3D fast low angle shot (FLASH) echo sequence magnetic resonance imaging. *Journal of Neurology*, 251(6), 740–746. <https://doi.org/10.1007/s00415-004-0420-5>
- Merker, B. (1983). Silver staining of cell bodies by means of physical development. *Journal of Neuroscience Methods*, 9(3), 235–241. [https://doi.org/10.1016/0165-0270\(83\)90086-9](https://doi.org/10.1016/0165-0270(83)90086-9)
- Mezer, A., Rokem, A., Berman, S., Hastie, T., & Wandell, B. A. (2016). Evaluating quantitative proton-density-mapping methods. *Human Brain Mapping*, 37(10), 3623–3635. <https://doi.org/10.1002/hbm.23264>
- Naidich, T. P., Duvernoy, H. M., Delman, B. N., Sorensen, A. G., & Haacke, E. M. (2009). *Duvernoy's atlas of the human brain stem and cerebellum: Duvernoy's atlas of the human brain stem and cerebellum: High-field MRI, surface anatomy, internal structure, vascularization and 3D sectional anatomy*. Springer.
- Nicoletti, V., Cecchi, P., Pesaresi, I., Frosini, D., Cosottini, M., & Ceravolo, R. (2020). Cerebello-thalamo-cortical network is intrinsically altered in essential tremor: Evidence from a resting state functional MRI study. *Scientific Reports*, 10(1), 16661. <https://doi.org/10.1038/s41598-020-73714-9>
- Novellino, F., Cherubini, A., Chiriaco, C., Morelli, M., Salsone, M., Arabia, G., & Quattrone, A. (2013). Brain iron deposition in essential tremor: A quantitative 3-tesla magnetic resonance imaging study. *Movement Disorders*, 28(2), 196–200. <https://doi.org/10.1002/mds.25263>
- Paraguay, I. B., França, C., Duarte, K. P., Diniz, J. M., Galhardoni, R., Silva, V., Iglesias, R., Bissoli, A. B., Menezes, J. R., Carra, R. B., Lepski, G., Barbosa, E. R., Ciampi de Andrade, D., Teixeira, M. J., & Cury, R. G. (2021). Dentate nucleus stimulation for essential tremor. *Parkinsonism & Related Disorders*, 82, 121–122. <https://doi.org/10.1016/j.parkreldis.2020.12.001>
- Paris-Robidas, S., Brochu, E., Sintès, M., Emond, V., Bousquet, M., Vandal, M., Pilote, M., Tremblay, C., di Paolo, T., Rajput, A. H., Rajput, A., & Calon, F. (2012). Defective dentate nucleus GABA receptors in essential tremor. *Brain*, 135(Pt 1), 105–116. <https://doi.org/10.1093/brain/awr301>

- Persson, N., Wu, J., Zhang, Q., Liu, T., Shen, J., Bao, R., Ni, M., Liu, T., Wang, Y., & Spincemaille, P. (2015). Age and sex related differences in subcortical brain iron concentrations among healthy adults. *NeuroImage*, 122, 385–398. <https://doi.org/10.1016/j.neuroimage.2015.07.050>
- Pietracupa, S., Bologna, M., Tommasin, S., Elifani, F., Vasselli, F., Paparella, G., Petsas, N., Berardelli, A., & Pantano, P. (2021). No evidence of iron deposition in essential tremor: A susceptibility-weighted imaging study. *Neurological Sciences*, 42, 4667–4672. <https://doi.org/10.1007/s10072-021-05173-7>
- Postuma, R. B., Berg, D., Stern, M., Poewe, W., Olanow, C. W., Oertel, W., Obeso, J., Marek, K., Litvan, I., Lang, A. E., Halliday, G., Goetz, C. G., Gasser, T., Dubois, B., Chan, P., Bloem, B. R., Adler, C. H., & Deuschl, G. (2015). MDS clinical diagnostic criteria for Parkinson's disease. *Movement Disorders*, 30(12), 1591–1601. <https://doi.org/10.1002/mds.26424>
- Pruthi, N., Kadri, P. A. S., & Ture, U. (2021). Fiber microdissection technique for demonstrating the deep cerebellar nuclei and cerebellar peduncles. *Operative Neurosurgery*, 20(2), E118–E124. <https://doi.org/10.1093/ons/opaa318>
- Shin, C., Lee, S., Lee, J. Y., Rhim, J. H., & Park, S. W. (2018). Non-motor symptom burdens are not associated with iron accumulation in early Parkinson's disease: A quantitative susceptibility mapping study. *Journal of Korean Medical Science*, 33(13), e96. <https://doi.org/10.3346/jkms.2018.33.e96>
- Shin, J. A., Kim, H.-S., Lee Kang, J., & Park, E.-M. (2020). Estrogen deficiency is associated with brain iron deposition via upregulation of hepcidin expression in aged female mice. *Neurobiology of Aging*, 96, 33–42. <https://doi.org/10.1016/j.neurobiolaging.2020.08.010>
- Slaughter, D. G., & Nashold, B. S., Jr. (1968). Stereotactic coordinates for the human dentate nucleus. *Confinia Neurologica*, 30(5), 375–384.
- Stebbins, G. T., Goetz, C. G., Burn, D. J., Jankovic, J., Khoo, T. K., & Tilley, B. C. (2013). How to identify tremor dominant and postural instability/gait difficulty groups with the movement disorder society unified Parkinson's disease rating scale: Comparison with the unified Parkinson's disease rating scale. *Movement Disorders*, 28(5), 668–670. <https://doi.org/10.1002/mds.25383>
- Sugiyama, A., Sato, N., Kimura, Y., Fujii, H., Maikusa, N., Shigemoto, Y., Suzuki, F., Morimoto, E., Koide, K., Takahashi, Y., Matsuda, H., & Kuwabara, S. (2019). Quantifying iron deposition in the cerebellar subtype of multiple system atrophy and spinocerebellar ataxia type 6 by quantitative susceptibility mapping. *Journal of the Neurological Sciences*, 407, 116525. <https://doi.org/10.1016/j.jns.2019.116525>
- Tellmann, S., Bludau, S., Eickhoff, S., Mohlberg, H., Minnerop, M., & Amunts, K. (2015). Cytoarchitectonic mapping of the human brain cerebellar nuclei in stereotaxic space and delineation of their co-activation patterns. *Frontiers in Neuroanatomy*, 9, 54. <https://doi.org/10.3389/fnana.2015.00054>
- Tishler, T. A., Raven, E. P., Lu, P. H., Altschuler, L. L., & Bartzokis, G. (2012). Premenopausal hysterectomy is associated with increased brain ferritin iron. *Neurobiology of Aging*, 33(9), 1950–1958. <https://doi.org/10.1016/j.neurobiolaging.2011.08.002>
- Wang, Y., Chen, Y., Wu, D., Wang, Y., Sethi, S. K., Yang, G., Xie, H., Xia, S., & Haacke, E. M. (2018). STategically acquired gradient Echo (STAGE) imaging, part II: Correcting for RF inhomogeneities in estimating T1 and proton density. *Magnetic Resonance Imaging*, 46, 140–150. <https://doi.org/10.1016/j.mri.2017.10.006>
- Ward, P. G. D., Harding, I. H., Close, T. G., Corben, L. A., Delatycki, M. B., Storey, E., Georgiou-Karistianis, N., & Egan, G. F. (2019). Longitudinal evaluation of iron concentration and atrophy in the dentate nuclei in friedreich ataxia. *Movement Disorders*, 34(3), 335–343. <https://doi.org/10.1002/mds.27606>
- Ward, R. J., Zucca, F. A., Duyn, J. H., Crichton, R. R., & Zecca, L. (2014). The role of iron in brain ageing and neurodegenerative disorders. *Lancet Neurology*, 13(10), 1045–1060. [https://doi.org/10.1016/s1474-4422\(14\)70117-6](https://doi.org/10.1016/s1474-4422(14)70117-6)
- Weiskopf, N., Suckling, J., Williams, G., Correia, M. M., Inkster, B., Tait, R., Ooi, C., Bullmore, E. T., & Lutti, A. (2013). Quantitative multi-parameter mapping of R1, PD(\*), MT, and R2(\*) at 3T: A multi-center validation. *Frontiers in Neuroscience*, 7, 95. <https://doi.org/10.3389/fnins.2013.00095>
- Wright, P. J., Mouglin, O. E., Totman, J. J., Peters, A. M., Brookes, M. J., Coxon, R., Morris, P. E., Clemence, M., Francis, S. T., Bowtell, R. W., & Gowland, P. A. (2008). Water proton T1 measurements in brain tissue at 7, 3, and 1.5 T using IR-EPI, IR-TSE, and MPRAGE: Results and optimization. *Magma*, 21(1–2), 121–130. <https://doi.org/10.1007/s10334-008-0104-8>
- Zhang, X., & Santaniello, S. (2019). Role of cerebellar GABAergic dysfunctions in the origins of essential tremor. *Proceedings of the National Academy of Sciences of the United States of America*, 116(27), 13592–13601. <https://doi.org/10.1073/pnas.1817689116>
- Zheng, W., Nichol, H., Liu, S., Cheng, Y.-C. N., & Haacke, E. M. (2013). Measuring iron in the brain using quantitative susceptibility mapping and X-ray fluorescence imaging. *NeuroImage*, 78, 68–74. <https://doi.org/10.1016/j.neuroimage.2013.04.022>
- Zhou, L., Chen, Y., Li, Y., Gharabaghi, S., Chen, Y., Sethi, S. K., Wu, Y., & Haacke, E. M. (2020). Intracranial iron distribution and quantification in aceruloplasminemia: A case study. *Magnetic Resonance Imaging*, 70, 29–35. <https://doi.org/10.1016/j.mri.2020.02.016>

## SUPPORTING INFORMATION

Additional supporting information can be found online in the Supporting Information section at the end of this article.

**How to cite this article:** Zhang, Y., Huang, P., Wang, X., Xu, Q., Liu, Y., Jin, Z., Li, Y., Cheng, Z., Tang, R., Chen, S., He, N., Yan, F., & Haacke, E. M. (2023). Visualizing the deep cerebellar nuclei using quantitative susceptibility mapping: An application in healthy controls, Parkinson's disease patients and essential tremor patients. *Human Brain Mapping*, 44(4), 1810–1824. <https://doi.org/10.1002/hbm.26178>